Near-infrared astrometry and photometry of Southern ICRF quasars

J. I. B. Camargo, G. Daigne, C. Ducourant, P. Charlot

A&A 437, 1135–1146 (2005)
DOI: 10.1051/0004-6361:20042426

Astronomy & Astrophysics

Near-infrared astrometry and photometry of Southern ICRF quasars⋆,⋆⋆,⋆⋆⋆

J. I. B. Camargo, G. Daigne, C. Ducourant, and P. Charlot

Observatoire Aquitain des Sciences de l'Univers, CNRS-UMR 5804, BP 89, 33270 Floirac, France
e-mail: camargo@obs.u-bordeaux1.fr

Received 23 November 2004 / Accepted 10 March 2005

Abstract. We present high quality astrometry, along with J, H, and K_s photometry, for 30 southern ICRF quasars observed with the ESO NTT/SOFI at La Silla. Our main purpose is to document the optical counterpart of ICRF quasars, by reporting their position in a stellar reference frame and their near-infrared photometry. Our investigation lies within the scope of extending the (radio) extragalactic reference frame into the optical range. An internal precision generally better than 10 mas was obtained in positioning the near-infrared counterpart of these quasars within their stellar surroundings. The actual astrometric accuracy is estimated from the departure between the observed and the radio (VLBI) positions of quasars, and is about 35 mas, mainly due to the statistical uncertainties of the stellar reference catalogue (UCAC2). The positional accuracy was improved to 25 mas for a subset of 14 quasars observed with extended fields of view, as obtained from mosaics of overlapping images. The 3-band photometry was achieved with a precision most often better than 0.04 mag, based on calibration with the 2MASS magnitudes. A spectral index α ($F_\nu \propto \nu^\alpha$) was derived from the observed quasar fluxes in the near-infrared. With a mean value $\langle\alpha\rangle = -1$, this spectral index does not show any significant correlation with the radio spectral index.

Key words. astrometry – infrared: general – methods: numerical – reference systems

1. Introduction

As of 1 January 1998, the International Celestial Reference Frame (ICRF) replaced the FK5 optical frame as the fundamental IAU celestial frame. The ICRF is a quasi-inertial reference frame based on the sub-milliarcsecond-accurate Very Long Baseline Interferometry (VLBI) positions of 212 extragalactic compact sources distributed over the entire sky (Ma et al. 1998). The ICRF is the prime realization of the IAU International Celestial Reference System (ICRS, Arias et al. 1995). In addition to these so called "defining" sources, positions for 294 "candidate" sources and 102 "other" sources were also published. This categorization was based on the observational history and the astrometric suitability of the sources. "Candidate" sources have the potential to be designated as defining sources in the future, as more observations or analysis improvements become available. "Other" sources were included in order to densify the frame, or because they may be useful for radio-optical frame ties (see e.g. Lestrade et al. 1999). Recently, positions in the ICRF for an additional 109 new sources were reported, based on VLBI observations accumulated since 1995 (Fey et al. 2004). Intrinsic source structure is also continuously monitored from VLBI observations in order to determine their suitability for reference-frame use (Fey et al. 1996; Fey & Charlot 1997, 2000; Ojha et al. 2004).

Realization of the ICRS at optical wavelengths is given by the HIPPARCOS Celestial Reference Frame (HCRF), whose principal axes coincide with those of the ICRF at the level of ±0.6 mas at J1991.25 with no global rotation at the level of ±0.25 mas/year (Kovalevsky et al. 1997). Due to the relatively low density of objects in the HCRF (about 3 objects per square degree), its densification is important to make access to the frame easier. Many authors (e.g. Urban et al. 1998; Monet et al. 1998, 2003; Zacharias et al. 2000; Camargo et al. 2001, 2003; Rapaport et al. 2001) have contributed to this densification from ground-based astrometry. The most recent achievement is the second US Naval Observatory (USNO) CCD Astrographic Catalogue (UCAC2) with positions and proper motions of about 48 million objects in the declination range −90° to +40° (Zacharias et al. 2004).

In the GAIA perspective, a prime realization of the ICRS at optical wavelengths may also be considered. Within this scenario, the coincidence between the optical and radio frames is a natural concern. Detailed imaging in the visible range of sources as faint as $V = 18-20$, a magnitude range that includes a large number of quasars, is out of reach for the ground-based

⋆ Based on observations collected with the ESO NTT/SOFI instrument at La Silla. ESO proposal 070.B-0553.

⋆⋆ Figures 12–26 are only available in electronic form at http://www.edpsciences.org

⋆⋆⋆ Tables 2–4 are also available in electronic form at the CDS via anonymous ftp to cdsarc.u-strasbg.fr (130.79.128.5) or via http://cdsweb.u-strasbg.fr/cgi-bin/qcat?J/A+A/437/1135

optical interferometers that are being built. The near-IR range is currently privileged for this task. With large optical telescopes and spatial phase-referenced imaging, objects as faint as $K_s = 19$ may be detectable in the future (Glindemann et al. 2003; Daigne & Lestrade 2003), so that an image resolution of some few mas will be possible for these objects. In this respect, single-dish astrometry of quasar fields in near-IR photometric bands is important for evaluating the feasibility of imaging with near-IR interferometry and for selecting initial candidates to the optical extension of the ICRF. Additionally, as compared to observations in the visible range, near-IR ones benefit from less atmospheric disturbances (scintillations, chromatic refraction) and lower Galactic extinction.

In this context, we conducted a pilot observing program of thirty ICRF quasars in the near-IR range with the ESO NTT in January 2003, as further described in the next section. Data processing and analysis are detailed in Sect. 3. Much effort was devoted to the astrometric reduction, first with an estimate of the camera field distortion and then with a global reduction of the observations in an extended-field mode (mosaics of overlapping images for fourteen ICRF quasars). Photometric results are given in Sect. 4 and astrometric results in Sect. 5. Discussion and concluding remarks are given in Sects. 6 and 7, respectively.

2. Observations

Our near-IR observations were carried out with the 3.5 m ESO NTT/SOFI located at La Silla, 70°43′54.272″ W 29°15′18.440″ S, during a 3-night run from 8 to 11 January 2003. Overall, a total of thirty ICRF quasars were observed generally when close to the local meridian, in order to minimize all systematic effects due to large airmass. The targets were selected according to two criteria: (i) the existence of a probable optical counterpart in the R band, as available in the USNOA-2.0 catalogue, and (ii) the existence of a sufficient number of UCAC reference stars in their vicinity. The second criterion was achieved by observing at low Galactic latitudes; see the sky distribution of the targets in Fig. 1. Furthermore, the declination range was limited to $\delta \leq -30°$ due to the sky coverage of the UCAC1 (Zacharias et al. 2000), since the UCAC2 was not available at the time the proposal for these near-IR observations was submitted to the ESO.

The SOFI instrument was used in its large field configuration with a resolution of 0.288″/pixel and an image size of 5′ × 5′. All quasars[1] were observed in a so-called "photometry" mode, where single images centered on the quasar positions were taken in each of the three near-IR photometric broad-band filters J, H, and K_s, the same as those of the Two Micron All-Sky Survey (2MASS), thus permitting proper calibration of our photometric measurements.

Due to the limited duration of our observing run, only fourteen quasars were observed in a so-called "astrometry" mode, which consists in observing extended fields centered on the quasar position. With a mosaic of 4 or 5 overlapping images, the field size was about twice that of a single-image area. The number of reference stars was larger, so positioning an extragalactic object in the UCAC2 stellar frame should be improved. Observations in the astrometry mode were performed with a narrow H-band filter[2] ($\lambda = 1.644/0.025\,\mu$m) to prevent saturation of the brightest reference stars. This filter is labelled "F" hereafter.

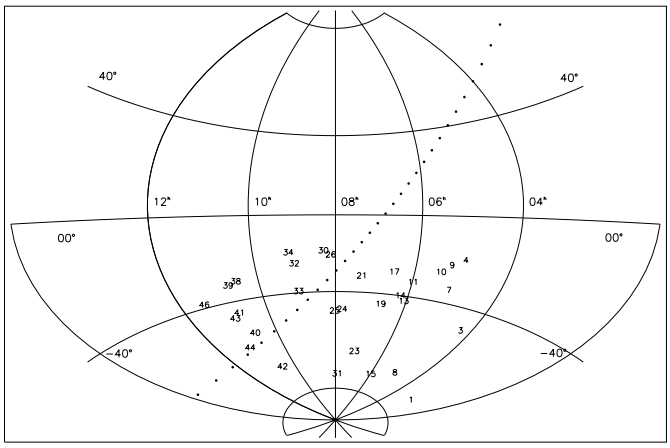

Fig. 1. Sky distribution of the observed ICRF quasars in equatorial coordinates. Each quasar is identified by an internal identification number listed in Col. 11 of Table 2. The dotted line indicates the Galactic equator.

Additionally, a dense stellar field (labelled 21 in Fig. 1) was also observed to determine the field distortion pattern (FDP) of the SOFI camera. This field comprised a mosaic of nine overlapping frames in the F filter only at low Galactic latitude ($l = 247.^{\circ}6$ and $b = -05.^{\circ}7$). All fields were observed with jitter offsets (see Hainaut et al. 2002, for further details) within a 10″ radius circle and an exposure time of 30 s per frame. Observations in each of the three broad-band J, H, and K_s filters were performed with seven jittered frames per image for a total exposure of 210 s. Observations in the narrow-band filter F were performed with 10 jittered frames for a total exposure of 300 s.

3. Image analysis and data reduction

The data analysis was carried out with the software ECLIPSE using the routine "jitter" (Devillard 1999) to perform sky subtraction and co-addition of the jittered frames, in order to obtain a final single-image in each filter. These single images were then treated with the DAOPHOT II package, to determine instrumental magnitudes and coordinates (x, y) for each detected object. The detection threshold was 7 times the rms value of background fluctuations (sky and readout noise). The coordinates (x, y) were determined by fitting a Moffat function of the form $(1 + z^2)^{-\beta}$ to the observed star profiles. In this function, $\beta = 2.5$ and $z^2 = x^2/\alpha_x^2 + y^2/\alpha_y^2 + \alpha_{xy}xy$, as given by Stetson (2000). The three parameters $\alpha_x, \alpha_y, \alpha_{xy}$ were adjusted in each image from a sub-sample of about 20 bright stars. The estimated diameter ($FWHM$) of the model point-spread function was generally in the range 0.7″−0.8″ during the three nights.

[1] Finding charts for all quasars can be provided on request to the authors.

[2] SOFI filter NB [Fe II].

The χ^2 value of the fit obtained for each object, generally in the range 0.6−2.5, is further used as a weighing function in the astrometric reduction (Sect. 3.2).

3.1. Photometry

The magnitudes were determined by finding the zero-points of each image for each filter. Each zero-point was calculated as the weighted mean of the differences between the instrumental and 2MASS magnitudes. An iterative procedure was used to eliminate 3-σ discrepant data and stopped when no further elimination was necessary.

The final precision of the magnitude is then given by

$$\sigma_{\rm mag} = \sqrt{\sigma_1^2 + \sigma_2^2}, \quad (1)$$

where σ_1 is the instrumental magnitude standard deviation, as given by DAOPHOT II, and σ_2 is the standard deviation of the zero-point determination.

3.2. Astrometry of single images

The initial astrometric reduction was carried out by using a linear model for the transformation between the measured pixel coordinates (x^i, y^i) of the reference stars and their standard coordinates (ξ^i, η^i):

$$\begin{aligned} \xi^i &= a_1(x^i - x_0) + b_1(y^i - y_0) + c_1 \\ \eta^i &= a_2(x^i - x_0) + b_2(y^i - y_0) + c_2. \end{aligned} \quad (2)$$

The standard coordinates of the reference stars are the gnomonic projection of their respective equatorial coordinates as given by the UCAC2 at the observation epoch, where the tangential point of the projection is chosen as the ICRF position of the observed quasar. With the quasar image close to the field center (x_0, y_0), c_1 and c_2 remain as small quantities.

Coefficients (a_1, b_1, c_1) and (a_2, b_2, c_2) in Eq. (2) were derived from a weighted least squares fit to the reference star coordinates. The weight for each star i was

$$w_i = (p_1^2 + p_2^2)_i^{-1}, \quad (3)$$

where $p_{1,i}$ is the position uncertainty of star i in the reference catalogue at the observation epoch, and $p_{2,i}$ stands for the position measurement error on the IR cell. Somewhat arbitrarily, $p_{2,i}$ was taken as $0.02'' \times \max(1.0, \chi_i^2)$, where χ_i^2 defines the quality of the fit for the star i (see above). Stars with discrepant coordinates (differences larger than 3-σ) were eliminated from the fit through an iterative procedure. When rejected in one of the photometric bands, a star was also rejected in the other bands. Equatorial coordinates of the detected objects in the UCAC2 stellar frame were then derived from Eq. (2) and by inverting the gnomonic projection.

3.3. Field distortion pattern (FDP) analysis

The transformation given by Eq. (2) was a first approach to astrometric reduction of the SOFI images. Clearly, corrections for an FDP have to be performed, in order to eliminate biases on the image coordinates. The dependence on the position in the image of the Observed minus Calculated (O−C) differences for the reference stars can be used to characterize the FDP. The effect of the FDP can then be seen through such systematic O−C deviations, as e.g. those shown in the upper right panel of Fig. 2.

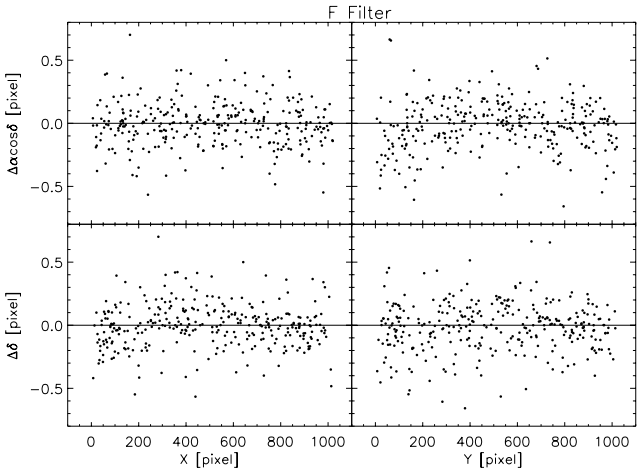

Fig. 2. O−C values for reference stars as a function of their image position in pixel units. No correction for the FDP was applied. Stars that were eliminated during the reduction process are not plotted.

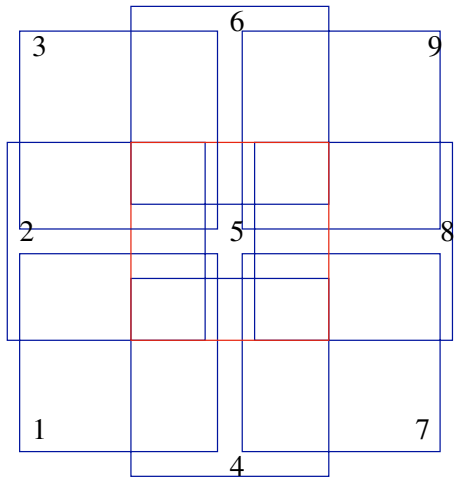

Fig. 3. Relative positions of the 9 mosaic images used for the FDP analysis. Each image is identified with a number. The total area is $10' \times 10'$.

The corrections for the FDP were determined from a mosaic of 9 overlapping images (see Fig. 3) observed in the F filter. The basic idea was to use the overlap to compare the positions of the same object as measured in different positions on the camera and then to determine systematic position shifts according to the location on the respective image area.

The initial astrometric reduction was first performed independently for each image as indicated above, in order to have initial spherical coordinates for each star. Then, new standard coordinates $\vec{\zeta_j^i} = (\xi_j^i, \eta_j^i)$ were determined for every star i in image j, using the centre of Image 5 (see Fig. 3) as the tangential point of the gnomonic projection, so that these new standard coordinates are on the plane given by the projection

Table 1. Individual components of the FDP matrices M_x and M_y.

0.3487	0.2974	0.0830	−0.0948	−0.3280
0.2242	0.2672	0.1491	−0.1421	−0.2748
0.1527	0.2257	0.1972	−0.1207	−0.2411
−0.0153	0.1485	−0.0033	−0.0612	−0.2045
−0.1166	−0.0813	0.0865	−0.0800	−0.1114
−0.4076	−0.3691	−0.2566	−0.2334	−0.2275
−0.1874	−0.2350	−0.1902	−0.0646	−0.0284
0.0268	0.0805	0.0939	0.2191	0.2306
−0.0196	0.0982	0.2612	0.3134	0.3001
−0.0872	−0.0415	0.0983	0.2134	0.2173

All values are expressed in pixel units, with the bottom leftmost elements of the matrices corresponding to the bottom leftmost corner of the image.

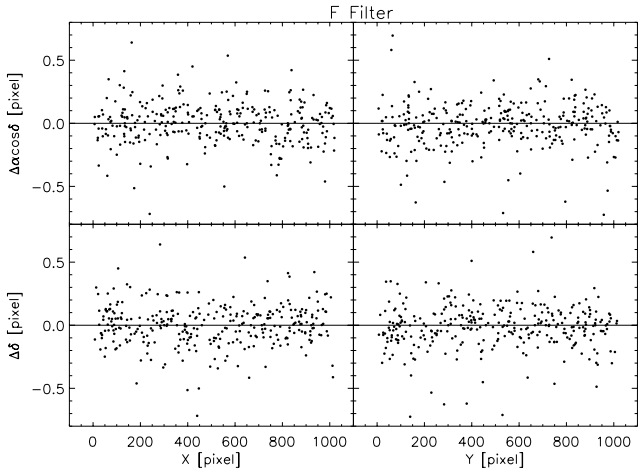

Fig. 4. O−C values for reference stars as a function of their image position, in pixel units. Correction for the FDP was applied. Stars that were eliminated during the reduction process are not plotted.

of Image 5. Relative rotations between them were previously corrected. Relative corrections for each star position were then derived as

$$\delta\overrightarrow{\zeta_j^i} = \overrightarrow{\zeta_j^i} - \langle\overrightarrow{\zeta_j^i}\rangle = (\delta\xi_j^i, \delta\eta_j^i), \quad (4)$$

where $\langle\overrightarrow{\zeta_j^i}\rangle$ is the average position of star i calculated over the overlapping images that contains this star. Equation (4) has been applied only to those objects observed in at least 4 images and with $12.0 \leq F \leq 17.0$.

The SOFI image was partitioned into a mosaic of 5×5 tiles with 200×200 pixels each. The average of the relative corrections in each tile defines the local FDP effect. In practice, the FDP is represented by two 5×5 matrices M_x and M_y with coefficients defined as

$$\begin{aligned} m_{xk} &= \langle\delta\xi_j^i\rangle_k \\ m_{yk} &= \langle\delta\eta_j^i\rangle_k, \end{aligned} \quad (5)$$

where the mean $\langle\rangle$ is calculated for each tile k, $k = 1\ldots25$. The FDP at a given place on the image can then be derived by interpolating the matrix coefficients using a bicubic spline.

The matrix coefficients m_{xk} and m_{yk} were calculated by using an iterative process, starting with $m_{xk} = 0$ and $m_{yk} = 0$ and then going back and forth between Eqs. (2) and (5) to refine the values of m_{xk} and m_{yk}. As a result of the gradual elimination of the FDP, the rms of the corrections $\delta\xi_j^i$ and $\delta\eta_j^i$ reached a minimum of 26 mas after 4 iterations, and the iterative procedure was stopped. The resulting matrices M_x and M_y are given in Table 1, while Fig. 4 shows the new O−C values as obtained from the astrometric analysis of single images described above after correcting for the FDP. Comparing with Fig. 2, one notices that the systematic effects are eliminated for the most part. The O−C values in Fig. 4 appear to be consistent with the nominal precision of the reference stars at the observation epoch (about 45 mas).

3.4. Astrometry of extended field observations

As mentioned above, fourteen ICRF quasars were observed in the "astrometry" mode, that is, with three or four additional images shifted with respect to the central one. The offsets are about half a single-image size, so that the extended field benefits from overlapping zones. This observing mode contributes to weakening the influence of positional errors of reference stars. It also brings some improvement when reference stars are not uniformly distributed over each image. With four offset images, the overall field is about twice as large as that of a single image.

The astrometric reduction of these extended fields was performed by using a global technique (Eichhorn 1960), also known as Block-Adjustment Method, similar to that used in the reduction of the Cape Photographic Catalogue plates (Zacharias 1988). Overall, this technique returns a set of positions in an essentially instrumental system, which should be aligned to the axes defined by a given reference frame afterwards. In this way, it is possible to benefit from a larger number of reference stars, while retaining the intrinsic imaging qualities of the instrument. This reduction method will not be explained further here, as it has been extensively described elsewhere (Teixeira et al. 1992, 1998). The application of this technique to extend a CCD field of view is also discussed in Yu et al. (2004).

4. Photometric results

Table 2 presents the photometric results obtained for our thirty ICRF quasars, along with further information available for these objects as retrieved from the literature. The detection threshold in the three near-IR photometric bands was $J = 20.8$, $H = 19.8$ and $K_s = 18.5$. All thirty quasars were detected in the three bands, and their magnitude distribution is shown in Fig. 5. With such a magnitude distribution, 17 quasars are not found in the 2MASS catalogue within a search radius of 1″ around the ICRF position. This figure goes down to 10 with a 5″ search radius. The magnitude precision, as derived

Table 2. Photometric data.

Literature data											Observational data								
												Magnitude			Flux				
ICRF name	c	z	6 cm	α_R	Type	M_B	B	V	R	IntID	MJD	J	H	K_s	J	H	K_s	α	σ_α
0312−770	C	0.223	0.56	0.3	Gal	−24.5	15.93	16.1	15.3	01a	52 648.02	14.67	14.04	13.06	2.22	2.55	3.97	−1.05	0.26
0431−512	C	0.557	0.59	−0.3	Quasar	−24.7	17.43	18.0	18.4	03p	52 649.02	16.88	16.03	15.17	0.29	0.40	0.57	−1.23	0.01
0511−220	C	1.296	0.87	0.1	Quasar	−25.4	19.34	19.5	19.6	04p	52 650.05	18.83	17.72	17.04	0.05	0.09	0.10	−1.27	0.01
0521−365	D	0.055	8.89	−0.5	BL Lac	–	12.15	14.6	11.4	07p	52 650.03	13.10	12.30	11.54	9.40	12.60	16.14	−0.98	0.12
0530−727	D	–	–	–	–	–	18.85	–	18.0	08p	52 648.05	16.39	15.41	14.47	0.46	0.72	1.08	−1.55	0.01
0528−250	O	2.765	0.85	−0.2	Quasar	−29.0	18.01	17.3	17.3	09a	52 649.04	16.09	15.71	15.39	0.60	0.55	0.47	0.44	0.01
0537−286	D	3.104	1.23	0.5	Quasar	−27.7	19.72	20.0	19.0	10a	52 650.07	17.76	16.94	16.24	0.13	0.18	0.21	−0.87	0.01
0614−349	C	–	–	−0.6	Other	–	19.98	18.0	16.8	11p	52 649.10	17.67	16.84	16.07	0.14	0.19	0.25	−1.05	0.00
0622−441	C	0.688	0.89	0.2	Quasar	−26.1	16.36	16.9	16.7	13p	52 650.10	15.81	15.09	14.28	0.78	0.97	1.30	−0.93	0.03
0629−418	D	1.416	0.74	0.5	Quasar	−26.0	18.18	19.3	18.2	14a	52 649.11	17.55	16.72	16.41	0.16	0.22	0.18	−0.22	0.03
0637−752	D	0.654	6.19	−0.1	Gal	−27.0	16.00	15.8	15.8	15p	52 650.12	14.82	14.31	13.60	1.92	1.98	2.43	−0.43	0.11
0646−306	C	0.455	1.06*	0.2	Quasar	−24.2	19.10	20.4*	18.8	17a	52 648.09	16.90	15.93	15.02	0.28	0.44	0.66	−1.56	0.00
0700−465	C	0.822*	0.64*	0.3	–	−24.3	18.57	19.5*	19.4	19a	52 649.15	15.67	14.82	13.94	0.88	1.23	1.76	−1.26	0.02
0700−465	C	0.822*	0.64*	0.3	–	−24.3	18.57	19.5*	19.4	19a	52 650.19	16.10	15.27	14.36	0.59	0.82	1.20	−1.29	0.02
0743−673	C	1.510	1.96	−1.0	Quasar	−28.6	16.15	16.4	15.9	23a	52 648.17	14.94	14.30	14.10	1.72	2.00	1.53	0.21	0.22
0809−493	C	–	–	−0.3	–	–	21.40	–	–	24p	52 650.30	19.29	18.32	17.28	0.03	0.05	0.08	−1.78	0.00
0823−500	C	–	–	–	–	–	–	–	–	25p	52 648.20	18.14	17.06	16.30	0.09	0.16	0.20	−1.46	0.02
0823−223	C	>0.910	0.78	0.5	BL Lac	–	15.88	16.2	15.8	26a	52 649.18	14.22	13.31	12.47	3.35	4.98	6.87	−1.31	0.09
0834−201	D	2.752	3.42	−0.3	Quasar	−27.9	19.09	19.4	18.8	30p	52 650.23	17.30	16.78	16.27	0.20	0.20	0.21	−0.09	0.00
0842−754	C	0.524	1.38	−0.7	Gal	−24.2	18.03	18.9	17.0	31p	52 650.32	16.76	15.94	15.16	0.32	0.44	0.58	−1.08	0.00
0919−260	O	2.300	2.38	0.2	Quasar	−27.7	18.63	18.4	18.0	32p	52 650.24	16.45	15.89	15.16	0.43	0.46	0.58	−0.54	0.02
0920−397	C	0.591	1.51	−0.2	Quasar	−24.4	18.54	18.8	17.7	33p	52 649.23	16.02	15.23	14.49	0.64	0.85	1.07	−0.94	0.01
0925−203	C	0.348	0.69	−0.2	Gal	−25.3	16.34	16.4	16.0	34p	52 649.21	15.48	14.74	14.02	1.04	1.33	1.64	−0.83	0.01
1048−313	C	1.429*	1.02*	−0.1	–	−25.7	–	19.4*	–	38p	52 649.25	18.29	17.43	16.88	0.08	0.11	0.12	−0.74	0.01
1101−325	C	0.354	0.73	−0.4	Gal	−25.5	17.11	16.3	15.5	39p	52 649.27	14.74	14.09	13.18	2.07	2.43	3.57	−0.99	0.18
1101−536	C	–	–	–	Quasar	–	17.82	17.9	16.4	40a	52 648.22	14.84	13.83	12.82	1.90	3.09	4.96	−1.74	0.01
1104−445	O	1.598	2.03	0.1	Quasar	−26.8	17.45	18.2	17.4	41a	52 648.25	16.20	15.39	15.07	0.54	0.73	0.62	−0.26	0.09
1105−680	C	0.588	1.37	0.3	Quasar	−23.6	17.89	18.4	17.9	42a	52 648.28	16.24	15.50	14.77	0.52	0.66	0.82	−0.83	0.00
1116−462	C	0.713	1.31	−0.4	Quasar	−26.0	17.25	17.0	16.5	43a	52 648.32	15.79	15.41	14.55	0.79	0.72	1.01	−0.44	0.10
1116−462	C	0.713	1.31	−0.4	Quasar	−26.0	17.25	17.0	16.5	43a	52 650.35	15.81	15.40	14.51	0.77	0.72	1.05	−0.56	0.11
1129−580	C	–	–	–	–	–	18.92	–	17.7	44a	52 649.33	15.73	15.01	14.39	0.83	1.04	1.17	−0.63	0.03
1144−379	C	1.048	2.22	−0.2	BL Lac	−27.7	17.23	16.2	16.7	46a	52 649.29	15.97	15.14	14.14	0.67	0.92	1.47	−1.43	0.05

Column 1: ICRF quasar identification; Col. 2: source category in the ICRF: Defining, Candidate or Other; Col. 3: redshift as given either by Archinal et al. (1997) or by the Veron-Cetty & Veron catalogue (Veron-Cetty & Veron 2003) (*); Col. 4: flux [Jy] at 6 cm as given either by Archinal et al. (1997) or by the Veron-Cetty & Veron catalogue (*); Col. 5: radio spectral index as given by Archinal et al. (1997); Col. 6: object type as given by Archinal et al. (1997); Col. 7: absolute B magnitude as given by the Veron-Cetty & Veron catalogue; Col. 8: B magnitude as given by the USNOB-1 catalogue (Monet et al. 2003); Col. 9: V magnitude as given either by Archinal et al. (1997) or by the Veron-Cetty & Veron catalogue (*); Col. 10: R magnitude as given by the USNOB-1 catalogue; Col. 11: internal identification – "p" for photometry mode, and "a" for astrometry mode; Col. 12: Modified Julian Date of the observation; Cols. 13−15: Observed J, H, and K_s magnitudes, respectively; Cols. 16–18: observed fluxes [mJy] in the J, H, and K_s filters, respectively; Col. 19: near-IR spectral indices, as derived from the observations in the J, H, and K_s filters; Col. 20: uncertainties of the spectral indices given by the preceding column.

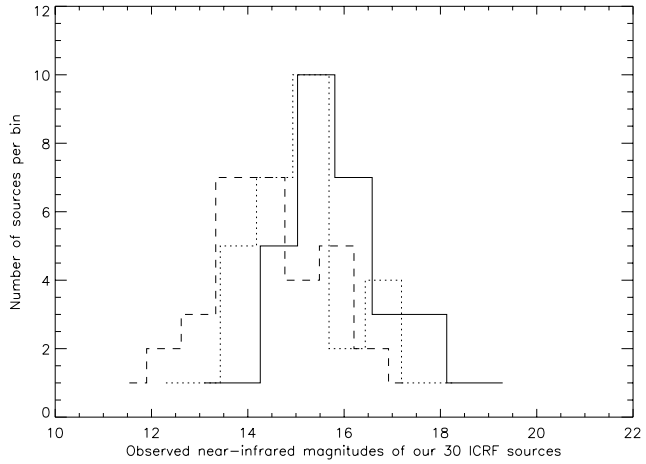

Fig. 5. Distribution of the observed quasar magnitudes in the three near-IR bands (full line: J, dotted line: H, dashed line: K_s).

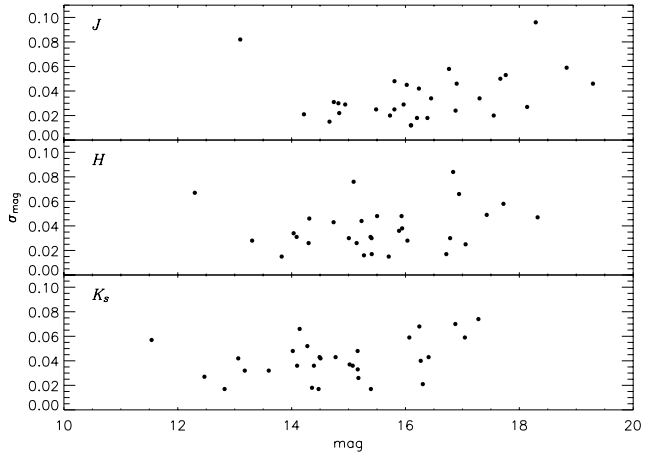

Fig. 6. Precision of the J, H, and K_s magnitudes as a function of the quasar magnitude.

from Eq. (1), is plotted in Fig. 6. The average precision is 0.037, 0.035, and 0.040 mag for the J, H, and K_s filters, respectively.

Near-IR spectral indices α, defined as $F_\nu \propto \nu^\alpha$, were inferred from the observed fluxes in the J, H, and K_s filters. These range from -1.8 to $+0.4$ with a mean value of about -1. We stress that these spectral indices do not refer to the emitted (rest-frame) frequencies ν from the quasars. The near-IR spectral indices are plotted in Fig. 7 as a function of the spectral indices in the radio range for these objects (see Table 2). The absence of significant correlation between the two sets of spectral indices has to be noticed.

Spectral energy distribution (SED) was estimated from the data in Table 2, considering radio, near-IR, and visible measurements. When available, flux at 11 cm or 15 cm as given by Archinal et al. (1997) was also used. The SEDs for all objects are available in the electronic version of this paper (Figs. 12 to 26). They show large amounts of energy being emitted in radio, near-IR, and optical wavelengths, as one would expect for AGNs. We stress that the radio and visible flux information do not correspond to the same epochs as the near-IR ones.

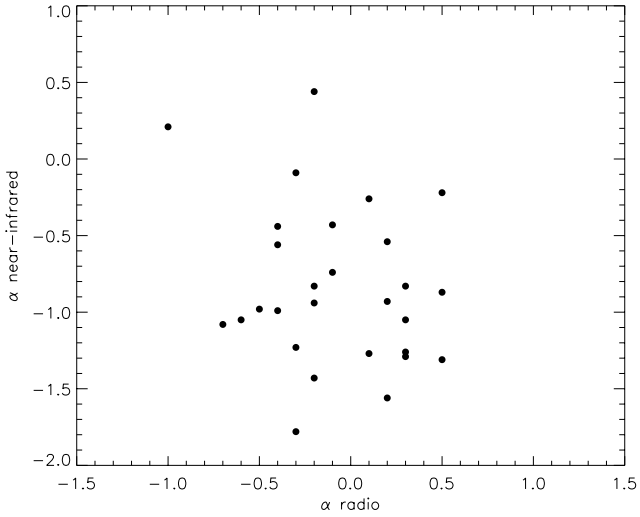

Fig. 7. Comparison of near-IR and radio spectral indices.

5. Astrometric results

Our astrometric results are presented in Tables 3 and 4, respectively obtained with the single-image analysis of all observed quasar fields and with the mosaics of overlapping images of fourteen selected quasar fields, with two of them observed twice.

5.1. Single images in the J, H, and K_s filters

Table 3 summarizes the astrometric results obtained from the analysis of single images (photometry mode). Figure 8 plots positional differences before and after the correction for the FDP (left and right panels, respectively). A better agreement with ICRF positions is clearly obtained after the correction for the FDP with larger improvement in declination.

The rms of the FDP-corrected positional differences is 35 mas in right ascension and 34 mas in declination, not considering the Fields 3, 4, 11, and 23, which show large discrepancies. The mean of these differences is 8 ± 7 mas and -6 ± 6 mas in right ascension and declination, respectively. Thus, no significant overall shift is present. These results are comparable to those presented in Assafin et al. (2003), obtained from the observations of 172 ICRF quasar fields with the Cerro Tololo Inter-American Observatory (CTIO) 0.9 m astrograph. The latter had $12' \times 12'$ fields, corresponding to four times the area of a NTT/SOFI field. It will be shown that better results are obtained from the NTT/SOFI when similar field sizes are involved.

Figure 9 shows the moduli of the positional differences as a function of the K_s magnitude. It is found that positions of similar quality are obtained over the whole magnitude range.

An important indicator of the achievable quality of the measurements is the internal coherence between the three photometric bands. As indicated in Cols. 7 and 8 of Table 3, this coherence is generally better than 10 mas. Thus, the NTT/SOFI appears to be an excellent instrument for narrow field astrometry.

Table 3. Astrometric data.

ICRF name	MJD	$\Delta\alpha*$	$\sigma_{\alpha*}$	$\Delta\delta$	σ_δ	$d_{\alpha*}$	d_δ	$e_{\alpha*}$	e_δ	N
0312−770	52 648.02	−23	21	47	21	10	5	47	11	5
0431−512	52 649.02	−238	183	333	174	24	11	0	0	3
0511−220	52 650.05	−56	47	141	61	11	3	0	0	3
0521−365	52 650.03	−36	27	−21	27	10	12	9	35	5
0530−727	52 648.05	43	44	5	46	6	5	79	27	4
0528−250	52 649.04	−7	10	5	10	4	4	24	38	6
0537−286	52 650.07	17	9	−14	9	6	6	45	37	7
0614−349	52 649.10	107	20	−190	19	18	15	11	105	4
0622−441	52 650.10	38	32	43	34	8	7	47	32	4
0629−418	52 649.11	1	22	−8	18	18	12	13	9	4
0637−752	52 650.12	−27	14	3	14	5	4	90	37	6
0646−306	52 648.09	−99	10	−21	10	4	3	154	33	6
0700−465	52 649.15	12	6	−23	5	6	16	28	39	9
0700−465	52 650.19	12	6	−23	5	6	16	31	26	10
0743−673	52 648.17	123	12	−43	15	2	3	53	84	8
0809−493	52 650.30	24	8	−34	8	5	16	52	48	14
0823−500	52 648.20	34	16	−10	17	4	6	56	71	11
0823−223	52 649.18	−25	11	21	11	5	8	60	122	18
0834−201	52 650.23	38	16	56	16	5	10	40	53	14
0842−754	52 650.32	18	12	31	13	8	5	50	43	15
0919−260	52 650.24	53	11	−53	11	6	1	42	46	9
0920−397	52 649.23	45	7	27	6	13	4	56	61	18
0925−203	52 649.21	−28	20	44	19	2	3	44	14	5
1048−313	52 649.25	41	12	−41	12	8	14	58	28	6
1101−325	52 649.27	−13	25	−58	20	8	4	86	102	4
1101−536	52 648.22	52	6	9	6	2	6	60	65	27
1104−445	52 648.25	−32	19	18	21	6	4	42	43	7
1105−680	52 648.28	25	5	−10	5	3	7	51	50	33
1116−462	52 648.32	35	4	−57	4	18	6	43	53	9
1116−462	52 650.35	35	4	−57	4	18	6	48	50	13
1129−580	52 649.33	−15	6	−6	6	8	6	59	52	22
1144−379	52 649.29	4	16	−49	15	7	7	53	30	6

All positional derived data are given in milliarcseconds [mas]. All ICRF positions are taken from Ma et al. (1998). $\alpha*$ stands for $\alpha\cos\delta$. Column 1: ICRF quasar identification; Col. 2: Modified Julian Date of the observation; Cols. 3 and 5: positional differences from the astrometric analysis of the observations made in the photometry mode, in the sense near-IR minus ICRF, in right ascension and declination, respectively. Near-IR positions are taken as the mean of those obtained from the J, H, and K_s bands; Cols. 4 and 6: precisions of the observed near-IR positions of the ICRF quasars, in right ascension and declination, respectively, as derived from the astrometric analysis of the observations made in the photometry mode. These precisions are the combined errors from each of the photometric filters; Cols. 7 and 8: standard deviations of the positional measurements in the J, H, and K_s filters in right ascension and declination, respectively; Cols. 9 and 10: mean of the standard deviations, as obtained from each of the photometric filters, of the differences observed minus calculated to the reference (UCAC2) stars in the photometry mode at the epoch of the observations; Col. 11: number of reference (UCAC2) stars used in the astrometric analysis of the observations made in the photometry mode.

5.2. Mosaics in the F filter

Table 4 summarizes the astrometric results derived from analysis of the fields observed in astrometry mode. As noticed in this table, improved quasar positions have been obtained, as compared to those from the single-image analysis (Cols. 3 and 5 versus Cols. 8 and 10). This table also shows that external

Table 4. Astrometric data.

		Single-image					Mosaic										
														$<(O-C)^2>^{\frac{1}{2}}$			
ICRF name	MJD	$\Delta\alpha*$	$\sigma_{\alpha*}$	$\Delta\delta$	σ_δ	N	$\Delta\alpha*$	$\sigma_{\alpha*}$	$\Delta\delta$	σ_δ	N	$c_{\alpha*}$	c_δ	$\alpha*$	δ	r_α	r_δ
		mas					mas					mas					
0312−770	52 648.02	−5	37	54	37	5	−41	18	11	23	10	53	91	58	33	1.18	0.72
0528−250	52 649.04	−4	17	−4	17	6	4	11	−11	10	14	31	20	20	35	0.53	1.00
0537−286	52 650.07	35	18	14	16	7	28	13	31	12	11	26	23	47	36	1.18	0.92
0629−418	52 649.11	38	39	31	33	4	30	9	−4	9	20	40	25	37	26	0.97	0.67
0646−306	52 648.09	−132	26	8	26	6	−44	7	9	6	31	35	36	35	33	1.00	1.03
0700−465	52 649.15	21	24	−17	23	9	−3	11	−1	9	23	38	27	46	33	0.92	0.80
0700−465	52 650.19	18	18	−3	18	10	8	12	−1	11	22	26	27	57	61	1.00	1.17
0743−673	52 648.17	128	22	−45	27	8	112	13	23	14	19	29	31	44	38	0.81	0.63
0823−223	52 649.18	−31	22	48	22	18	−28	9	25	10	46	26	28	57	69	0.90	1.06
1101−536	52 648.22	46	11	17	11	27	33	6	36	6	81	25	21	46	73	0.96	1.46
1104−445	52 648.25	−42	34	25	38	7	8	8	9	8	32	30	23	49	53	1.11	1.26
1105−680	52 648.28	32	8	29	8	33	25	5	4	5	88	27	27	67	54	1.46	1.20
1116−462	52 648.32	46	22	−52	22	9	22	7	−42	7	42	25	25	39	53	0.93	1.23
1116−462	52 650.35	40	21	−28	21	13	18	7	−26	7	42	26	30	45	51	1.07	1.19
1129−580	52 649.33	−43	13	33	13	22	−30	4	14	4	131	30	26	54	56	1.10	1.10
1144−379	52 649.29	12	30	−29	27	6	28	13	−51	11	16	30	29	39	43	0.76	1.02

All positional derived data are given in milliarcseconds [mas]. All ICRF positions are taken from Ma et al. (1998). $\alpha*$ stands for $\alpha\cos\delta$. Only results in the F filter are concerned. Column 1: ICRF quasar identification; Col. 2: Modified Julian Date of the observation; Cols. 3 and 5: positional differences from the astrometric analysis of the single central image, in the sense near-IR minus ICRF, in right ascension and declination, respectively; Cols. 4 and 6: precisions from the astrometric analysis of the single central image, of the observed near-IR positions of the ICRF quasars, in right ascension and declination, respectively; Col. 7: number of reference (UCAC2) stars used in the astrometric analysis of the single central images; Cols. 8 and 10: positional differences from the reduction in astrometry mode, in the sense near-IR minus ICRF, in right ascension and declination, respectively; Cols. 9 and 11: precisions of the observed near-IR positions in the astrometry mode of the ICRF quasars in right ascension and declination, respectively; Col. 12: number of reference (UCAC2) stars used in the astrometry mode; Cols. 13 and 14: internal precision as obtained from the positions of stars in overlapping regions, in right ascension and declination, respectively; Cols. 15 and 16: rms of the differences observed minus calculated to the reference (UCAC2) stars in the astrometry mode at the epoch of the observations, in right ascension and declination, respectively; Cols. 17 and 18: ratio between the values provided by Cols. 15 and 16 and the respective nominal standard deviations propagated to the epoch of the observations for the reference stars, in right ascension and declination, respectively.

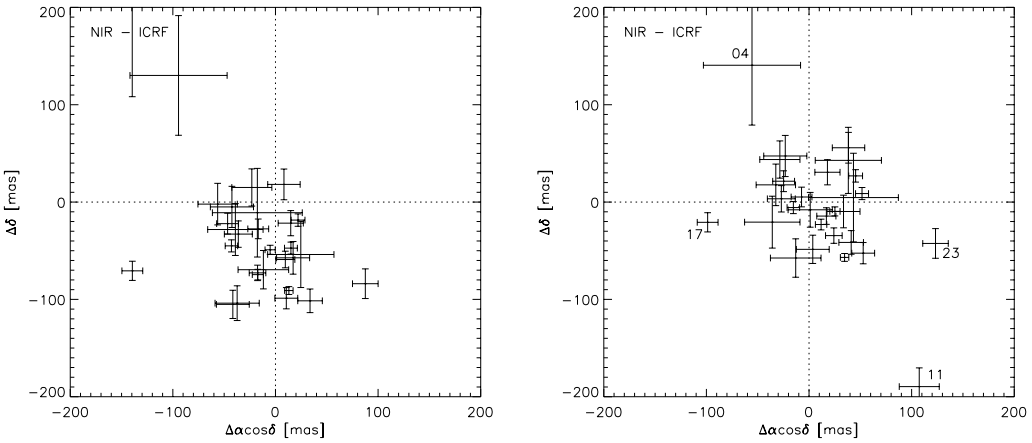

Fig. 8. Differences in the sense near-IR minus ICRF, before (*left panel*) and after (*right panel*) correcting for the FDP. The near-IR positions are the mean of the J, H, and K_s positions, with errors as in Cols. 4 and 6 of Table 3. In the right panel, the four largest differences have the internal identification numbers of their corresponding objects indicated. Note that the difference for Field 3 falls outside the limits of the figure.

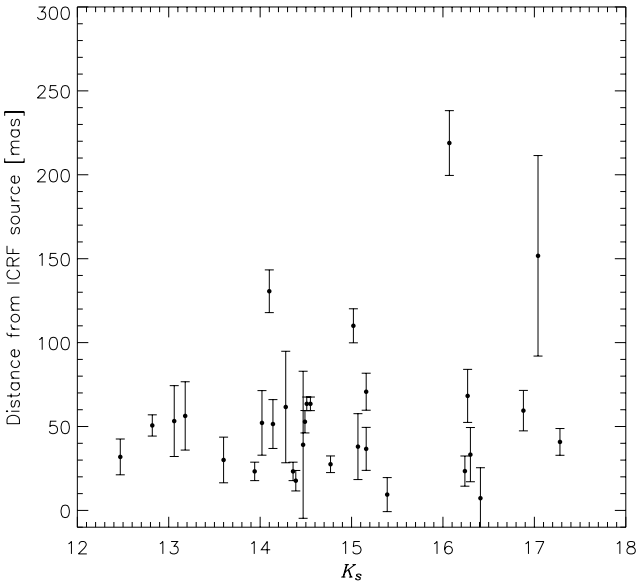

Fig. 9. Distance moduli between the near-IR and ICRF positions as a function of the K_s magnitude.

astrometric errors are dominated by the positional uncertainties of the reference stars (Cols. 17 and 18). A plot comparing the near-IR and ICRF positional differences obtained from the two analyses is shown in Fig. 10. From the mosaics, the mean of these differences is 7 ± 7 mas in right ascension and 0 ± 7 mas in declination. These shifts are smaller than those found in the single-image analysis.

The rms of the differences between near-IR and ICRF positions is also printed in both panels of Fig. 10. As expected, these values are smaller for the mosaics, since they benefit from a larger number of reference stars than the single images. However, the gain factor is smaller than the square root of the increased number of reference stars (factors of 1.32 and 1.24 in right ascension and declination, respectively, instead of about 1.4). This may result from systematic offsets in the UCAC2.

5.3. Revisiting the FDP and the reference catalogue

Columns 13 to 16 of Table 4 show that the positional internal coherence of the measurements within the images is frequently better than the agreement with the UCAC2 at the observation epoch. The same conclusion is also inferred from Cols. 17 and 18 of the same table. This implies that the measurement uncertainties are smaller than the nominal uncertainties of the reference stars.

Bearing this in mind, we applied the astrometric analysis given by Eq. (2) only to the central images in the F filter of each of the fourteen fields observed in the astrometry mode. Reference star positions were previously modified according to the corrections obtained from analysis of the mosaics. The derived rms of the positional differences near-IR minus radio for the observed ICRF quasars were 27 and 28 mas in right ascension and declination, respectively, excluding Fields 17 and 23. As expected, these values are better than those previously obtained from the concerned single images (33 and 31 mas, respectively). This indicates good performance of the FDP model and also that the positions of the reference stars are improved on the average.

Taking these corrections into consideration, the dispersion of the O−C differences is naturally attenuated, and it becomes easier to visualise the FDP effects. This is illustrated in Fig. 11, which shows the uncorrected and the FDP-corrected positional scatter in the same way as originally in Figs. 2 and 4. The pattern shown in the left panel of Fig. 11 is the intrinsic FDP effect. The right panel shows more clearly that most of its signature was eliminated.

5.4. Notes on individual ICRF quasars

0431−512 (03p) Only three reference stars. Quasar not detected in the F filter.

0511−220 (04p) Only three reference stars. Quasar not detected in the F filter.

0530−727 (08p) Only four reference stars.

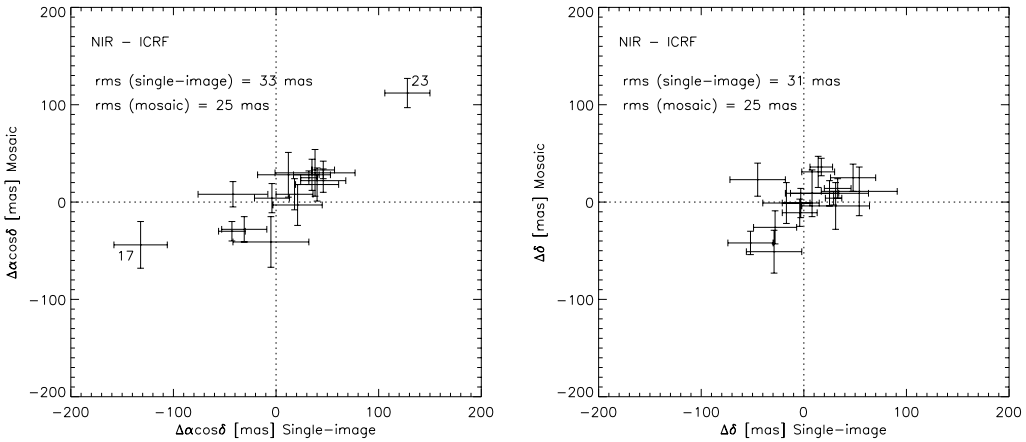

Fig. 10. Comparison between the astrometric results from single-image (horizontal axes) and mosaic (vertical axes) modes in the *F* filter. In the left panel, the two largest differences have the internal identification numbers of their corresponding objects indicated. These were not considered for calculating the rms values printed in each panel.

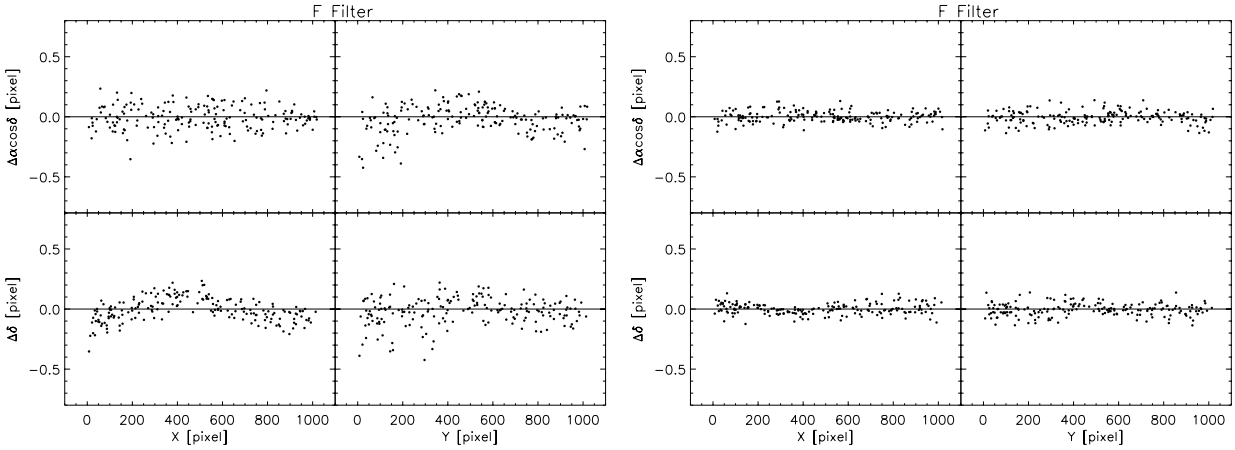

Fig. 11. Comparison of the uncorrected and FDP-corrected positional scatter from the single-image treatment. The reference (UCAC2) star positions were modified according to improvements provided by the global reduction technique. *Left panel*: without correction for the FDP. *Right panel*: with correction for the FDP.

0614−349 (11p) Only four reference stars. A high value obtained to the χ^2 fit parameter from DAOPHOT II indicates that the PSF profile fit to this source did not work well. This object is classified as "Pair of Galaxies" in the SIMBAD database. Its ICRF positional precision is 66 mas in $\alpha\cos\delta$ and 39 mas in δ.
0622−441 (13p) Only four reference stars.
0646−306 (17a) The significant difference $\Delta\alpha\cos\delta$ obtained from the single-image reduction in the *F* filter (−132 mas) is clearly reduced with the extended field reduction (−44 mas).
0743−673 (23a) The significant difference $\Delta\alpha\cos\delta$ (128 mas) obtained from the single-image reduction in the *F* filter persists in the extended field reduction (112 mas).
0809−493 (24p) A revised VLBI position of this source is given in Fey et al. (2004). As compared with that given by Ma et al. (1998), a difference of 6 mas in right ascension is found, whereas Table 3, Col. 3, shows a difference of 24 mas to this source. Although these differences are within the accuracies of their radio and near-IR measurements, ±8 mas and ±35 mas respectively, it is interesting to notice that both have the same sign.
1101−325 (39p) Only four reference stars.

6. Discussion

In preparation for the next astrometric missions, visible/near-IR astrometry and photometry of ICRF quasars is important for identifying the best candidates for an extension of the ICRF in the optical range. Also worth emphasizing is its importance for checking the positional accuracy of extensions of the current stellar reference frame to fainter magnitudes, as well as for studies related to the radio-optical frame tie (da Silva Neto et al. 2002; Assafin et al. 2003). With less atmospheric disturbances than in the visible range, narrow-field astrometry of ICRF quasars in the near-IR reaches an internal precision generally better than 10 mas (see Table 3). However, the actual position accuracy is significantly worse, and mainly affected by two major uncertainties: (i) the quality of the image mapping and its FDP correction, and (ii) statistical errors due to the limited number of reference stars and their position uncertainties.

A model for the FDP has been obtained with overlapping fields in a narrow band filter at 1.644 μm. At the epoch of our observations, the FDP reached 0.4 pixel (or 115 mas) in the cell corners, and sub-0.1 pixel effects may not have been

completely corrected (see O−C residuals in Fig. 11). Improvements in this domain should be possible in future observing runs, due to a re-alignment of the SOFI camera (Billères 2004, private communication). Additionally, astrometry in the newly-implemented J_s filter will be helpful for such modelling due to the larger dynamic range available in this band and the adjustement of the (active) primary mirror in this same band.

Positional accuracy is limited at first by the internal precision of the instrument used to perform the astrometric observations. While in an ideal situation it is the only limiting error, there are often systematic errors that dominate the reduction process in actual measurements. In our case, the internal positional precision of the quasars observed with the NTT/SOFI is generally better than 10 mas, but uncertainties in the reference stellar frame dominate the error budget. Enlarging the field of view by mosaics of overlapping images is one way to reduce such systematic effects, as presented in this paper. This effort should be pursued further with observations on even larger fields, in order to bring the error contribution from the reference stars down to a lower level than that of the internal astrometric precision of the NTT/SOFI. Also of interest is that the overlapping of images may be used to link closely ICRF sources and obtain improved stellar positions and proper motions from multi-epoch observations.

Enlarging the field of view to profit from a larger number of reference stars may represent a time-consuming operation to the NTT/SOFI, so that one envisages the construction of a denser and more accurate stellar frame as performed by a different instrument. This represents a twofold process that has long been common practice in quasar optical astrometry, with traditionally wide field photographic plates, on the one hand, and narrow field CCD image, on the other (see e.g. Zacharias et al. 1999). A similar densification process could be now obtained with the Wide Field Imager (WFI) mounted at the Cassegrain focus of the 2.2-m MPG/ESO telescope. The WFI has a $34' \times 33'$ field area, enough to contain about 200 UCAC2 stars, therefore making a refined selection of reference stars for the astrometric analysis possible. Although a more detailed investigation is needed, it is likely that the 10 mas internal precision of the NTT/SOFI may be reached for the positional accuracy with this observing procedure in the future.

It is to be noted that a large departure (>100 mas) in right ascension between the near-IR and ICRF positions was found out to Field 23 from both single-image and extended field analyses. In the radio, the corresponding target (0743−673) now has a sub-milliarcsecond-accurate improved VLBI position (Fey et al. 2004) that differs only at the sub-mas level from the original ICRF position in Ma et al. (1998). Thus, it is unlikely that the ICRF positional error contributes significantly to the observed >100 mas discrepancy. While physical effects (different spatial location for the optical and radio emission) may play a role, we cannot go further in explaining this discrepancy with the present 25 mas accuracy of our near-IR observations. Future improved accuracies down to the 10 mas level, as discussed above, should provide deeper insight into this matter.

7. Conclusion

We have reported results of near-IR astrometry and photometry for 30 southern ICRF quasars. Based on single-image analysis, the positional accuracy of our measurements is about 35 mas, which compares favourably to the best ground-based visible/near-IR measurements published so far. When observing with the mosaic mode's larger field of view, the positional accuracy is improved to 25 mas. Because of the excellent metrological capabilities of the NTT/SOFI (10 mas internal positional precision), even better accuracy could be obtained if denser stellar frames were available around our targets.

Astrometric results derived from each of the three photometric filters were found to be equivalent within the involved errors. Instrumental magnitudes were calibrated with the 2MASS catalogue and with precision better than 0.04 mag. The magnitudes of our 30 quasars range from 11.5 to 17.3 in the K_s band. Within this range, the uncertainty of the near-IR position and the difference from the ICRF position are independent of the magnitude.

Pursuing this investigation further would require improved stellar reference frames around ICRF quasars. Astrometric accuracies at the level of 10 mas in the optical range are foreseeable in the future, and would imply a more physical approach when comparing radio and optical positions, as this level of accuracy corresponds to the typical size of extended structures observed in quasar radio maps.

Acknowledgements. The authors acknowledge partial financial support from the (OASU/L3AB). The authors also acknowledge the suggestions from an anonymous referee. This publication makes use of data products from the Two Micron All-Sky Survey, which is a joint project of the University of Massachusetts and the Infrared Processing and Analysis Center/California Institute of Technology, funded by the National Aeronautics and Space Administration and the National Science Foundation. This research has also made use of the SIMBAD database operated at CDS, Strasbourg, France. This publication makes use of numerical codes from Numerical Recipes in FORTRAN 77. J. I. B. Camargo is supported by CNPq – Brazil.

References

Archinal, B. A., Arias, E. F., Gontier, A.-M., & Mercuri-Moreau, C. 1997, in Definition and Realization of the International Celestial Reference System by VLBI Astrometry of Extragalactic Objects, IERS Tech. Note 23, Paris: Obs. Paris, ed. C. Ma, & M. Feissel, III–11

Arias, E. F., Charlot, P., Feissel, M., & Lestrade, J.-F. 1995, A&A, 303, 604

Assafin, M., Zacharias, N., Rafferty, T. J., et al. 2003, AJ, 125, 2728

Camargo, J. I. B., Teixeira, R., Benevides-Soares, P., & Ducourant, C. 2001, A&A, 375, 308

Camargo, J. I. B., Ducourant, C., Teixeira, R., et al. 2003, A&A, 409, 361

da Silva Neto, D. N., Andrei, A. H., Vieira, R. V., & Assafin, M. 2002, AJ, 124, 612

Daigne, G., & Lestrade, J.-F. 2003, A&A, 406, 1167

Devillard, N. 1999, in Astronomical Data Analysis Software and Systems VIII, ed. D. M. Mehringer, R. L. Plante, & D. A. Roberts (San Francisco: ASP), ASP Conf. Ser., 172, 333

Eichhorn, H. 1960, Astron. Nach., 285, 233

Fey, A. L., & Charlot, P. 1997, ApJS, 111, 95
Fey, A. L., & Charlot, P. 2000, ApJS, 128, 17
Fey, A. L., Clegg, A. W., & Fomalont, E. B. 1996, ApJS, 105, 299
Fey, A. L., Ma, C., Arias, E. F., et al. 2004, AJ, 127, 3587
Glindemann, A., Algomedo, J., Amestica, R., et al. 2003, in Interferometry for Optical Astronomy II, ed. W. Traub, Proc. SPIE, 4838, 89
Hainaut, O., Pompei, E., Billères, M., et al. 2002, SOFI User's Manual, La Silla Observatory – Doc. No. LSO-MAN-ESO-40100-0004
Kovalevsky, J., Lindegren, L., Perryman, M. A. C., et al. 1997, A&A, 323, 620
Lestrade, J.-F., Preston, R. A., Jones, D. L., et al. 1999, A&A, 344, 1014
Ma, C., Arias, E. F., Eubanks, T. M., et al. 1998, AJ, 116, 516
Monet, D., Bird, A., Canzian, B., et al. 1998, in USNO–A V2.0, A Catalog of Astrometric Standards
Monet, D., Levine, S. E., Canzian, B., et al. 2003, AJ, 125, 984
Ojha, R., Fey, A. L., Johnston, K. J., et al. 2004, AJ, 127, 3609
Rapaport, M., Le Campion, J.-F., Soubiran, C., et al. 2001, A&A, 376, 325
Stetson, P. B. 2000, DAOPHOT User's Manual
Teixeira, R., Réquième, Y., Benevides-Soares, P., & Rapaport, M. 1992, A&A, 264, 307
Teixeira, R., Camargo, J. I. B., Benevides-Soares, P., & Réquième, Y. 1998, A&A, 333, 1107
Urban, S. E., Corbin, T. E., Wycoff, G. L., et al. 1998, AJ, 115, 1212
Veron-Cetty, M. P., & Veron, P. 2003, A&A, 412, 399
Yu, Y., Tang, Z. H., Li, J. L., Wang, G. L., & Zhao, M. 2004, AJ, 128, 911
Zacharias, N. 1988, Mapping the Sky: Past Heritage and Future Directions: Proc. of the 133rd Symposium of the International Astronomical Union, held in Paris, France, 1−5 June 1987, ed. S. Debarbat, International Astronomical Union, Symp., 133 (Dordrecht: Kluwer Academic Publishers), 201
Zacharias, N., Zacharias, M. I., Hall, D. M., et al. 1999, AJ, 118, 2511
Zacharias, N., Urban, S. E., Zacharias, M. I., et al. 2000, AJ, 120, 2131
Zacharias, N., Urban, S. E., Zacharias, M. I., et al. 2004, AJ, 127, 3043

Online Material

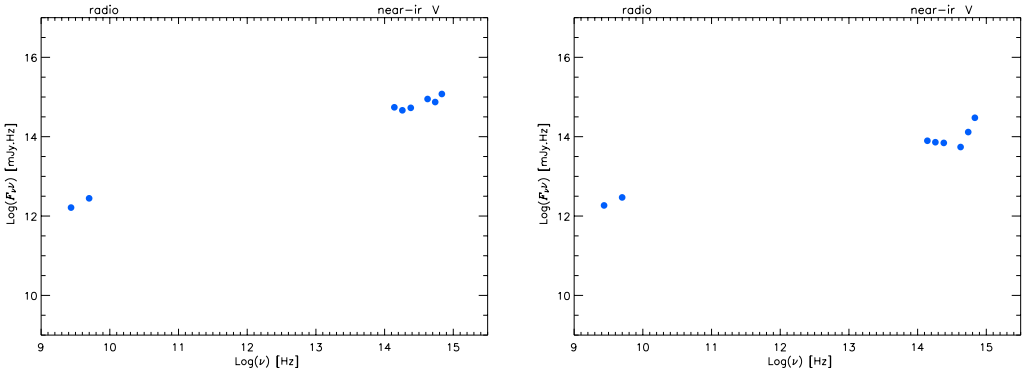

Fig. 12. SED. *Left*: 0312−770 (01a). *Right*: 0431−512 (03p).

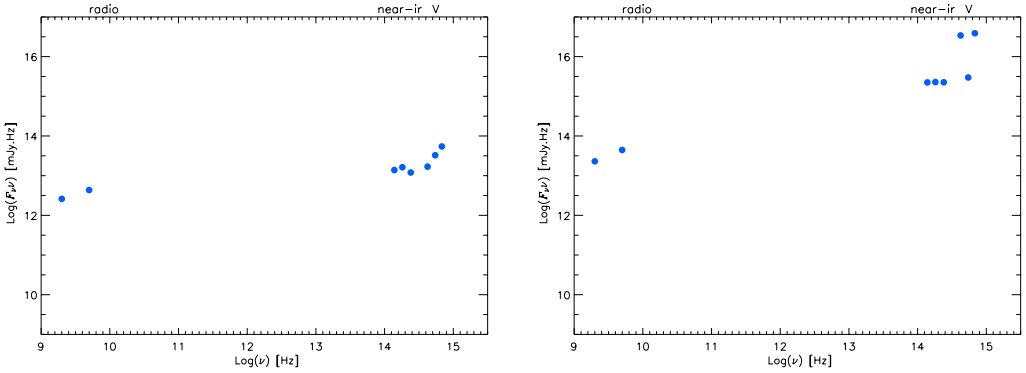

Fig. 13. SED. *Left*: 0511−220 (04p). *Right*: 0521−365 (07p).

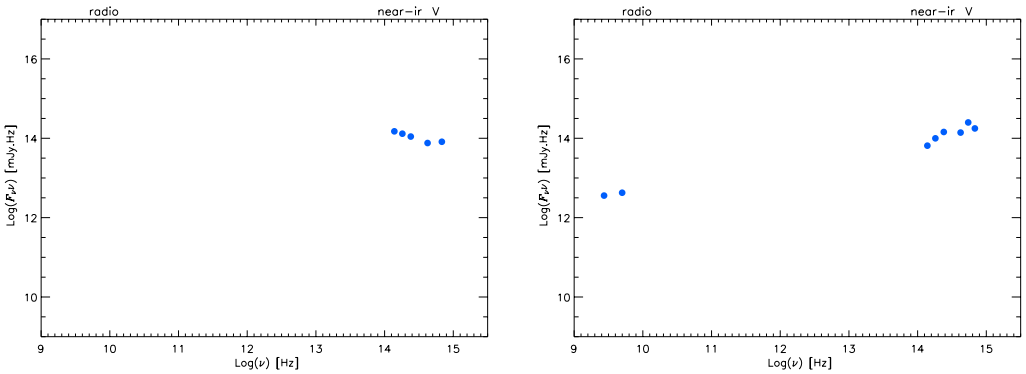

Fig. 14. SED. *Left*: 0530−727 (08p). *Right*: 0528−250 (09a).

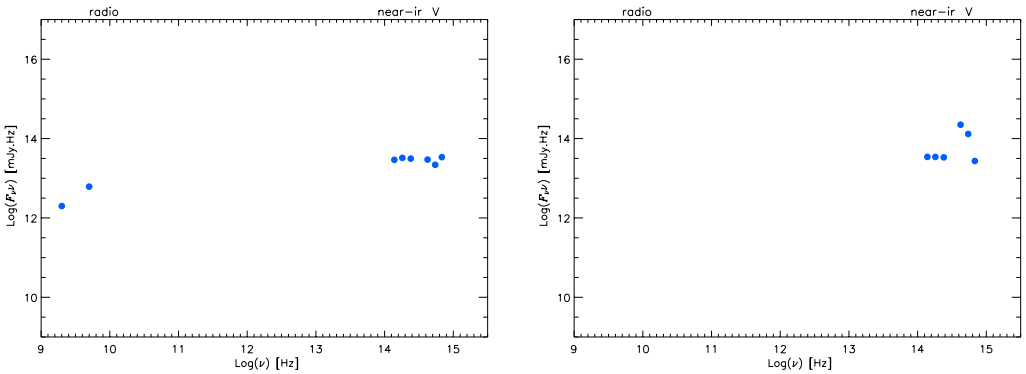

Fig. 15. SED. *Left*: 0537−286 (10a). *Right*: 0614−349 (11p).

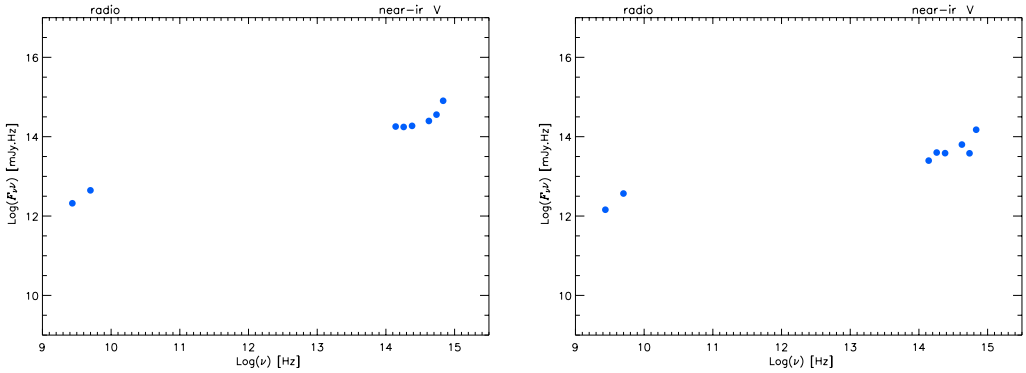

Fig. 16. SED. *Left*: 0622−441 (13p). *Right*: 0629−418 (14a).

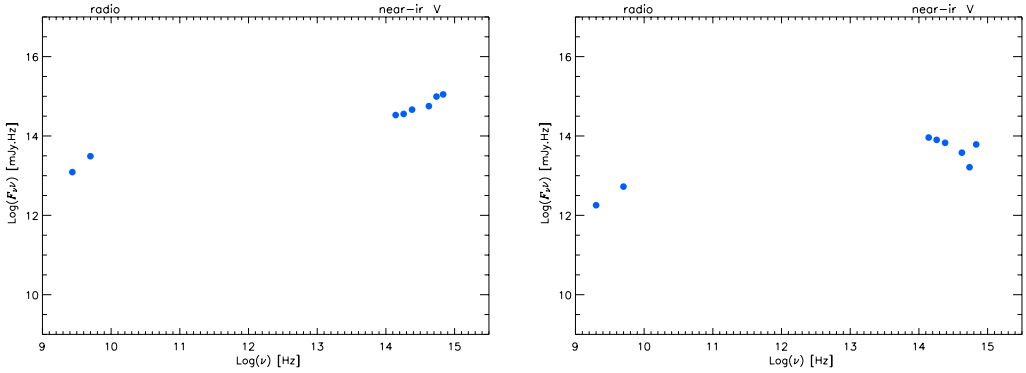

Fig. 17. SED. *Left*: 0637−752 (15p). *Right*: 0646−306 (17a).

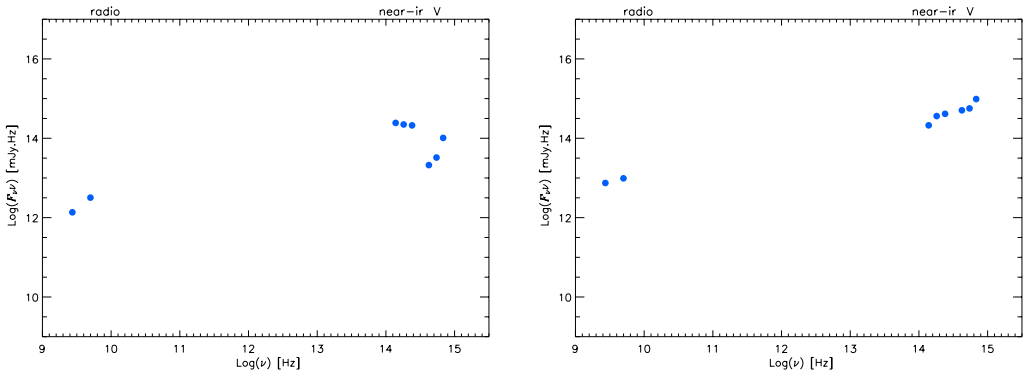

Fig. 18. SED. *Left*: 0700−465 (19a). *Right*: 0743−673 (23a).

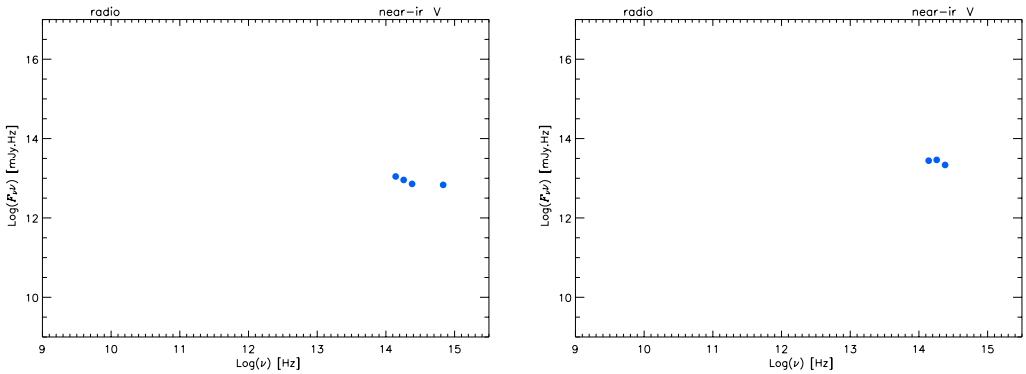

Fig. 19. SED. *Left*: 0809−493 (24p). *Right*: 0823−500 (25p).

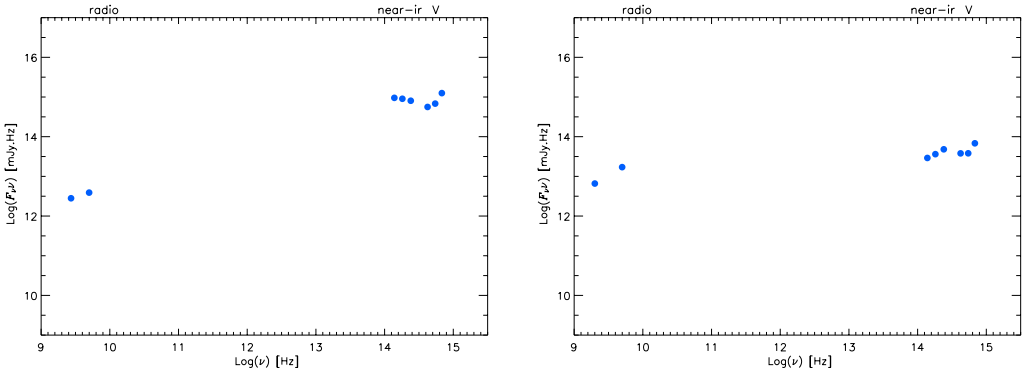

Fig. 20. SED. *Left*: 0823−223 (26a). *Right*: 0834−201 (30p).

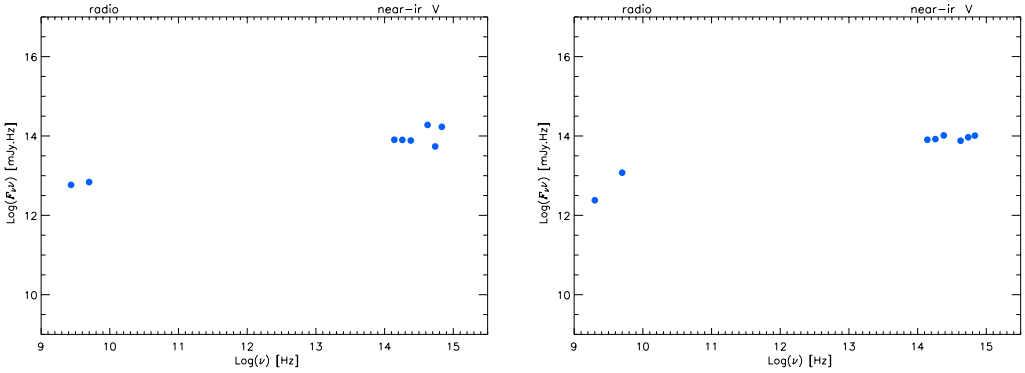

Fig. 21. SED. *Left*: 0842−754 (31p). *Right*: 0919−260 (32p).

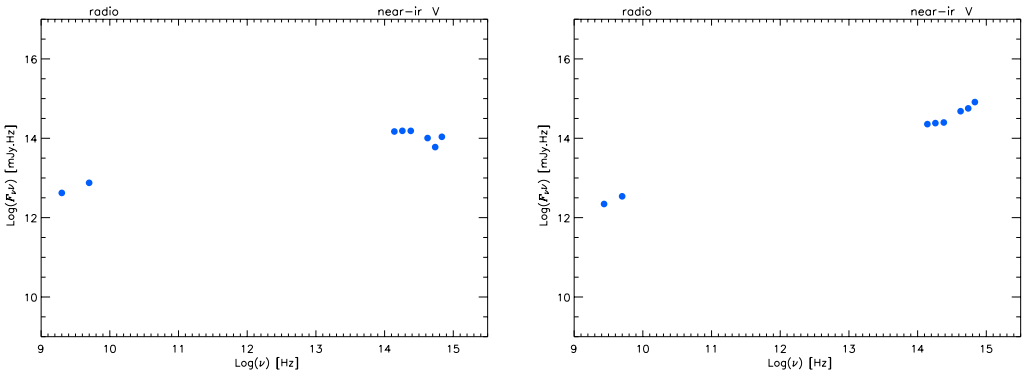

Fig. 22. SED. *Left*: 0920−397 (33p). *Right*: 0925−203 (34p).

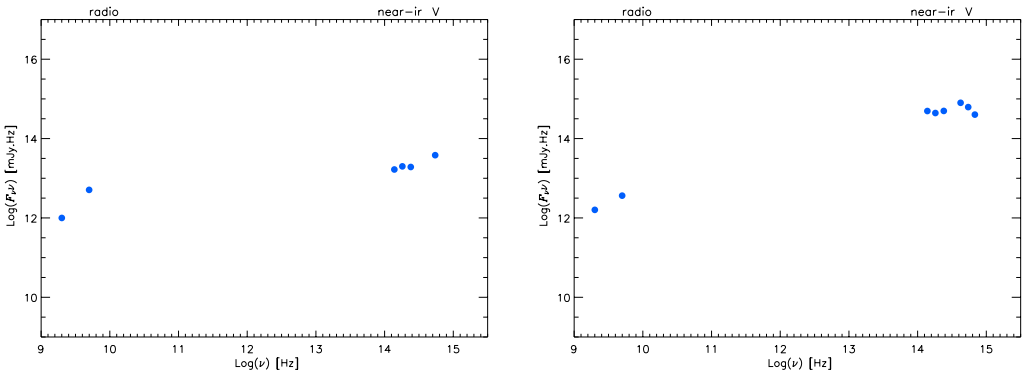

Fig. 23. SED. *Left*: 1048−313 (38p). *Right*: 1101−325 (39p).

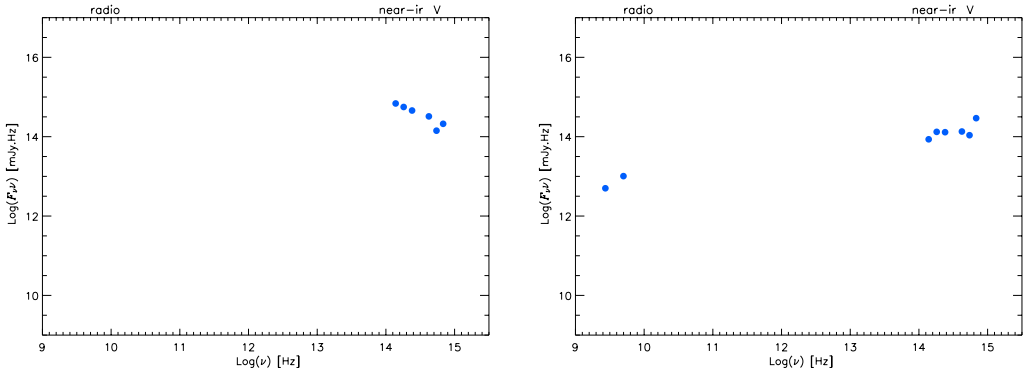

Fig. 24. SED. *Left*: 1101−536 (40a). *Right*: 1104−445 (41a).

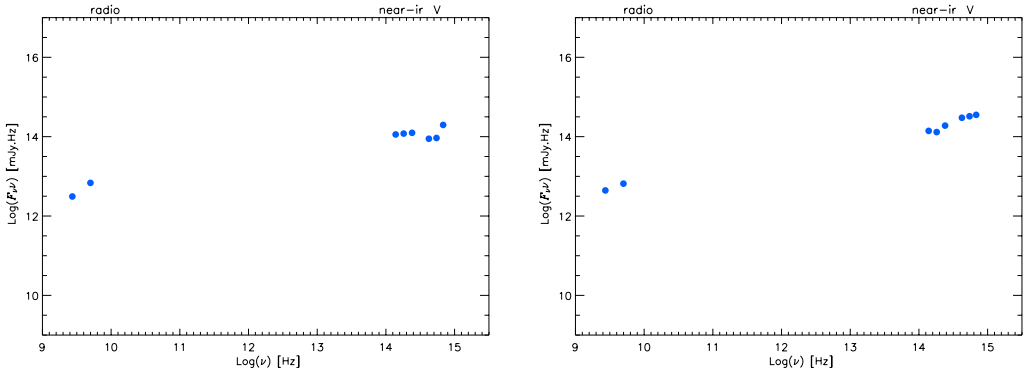

Fig. 25. SED. *Left*: 1105−680 (42a). *Right*:1116−462 (43a).

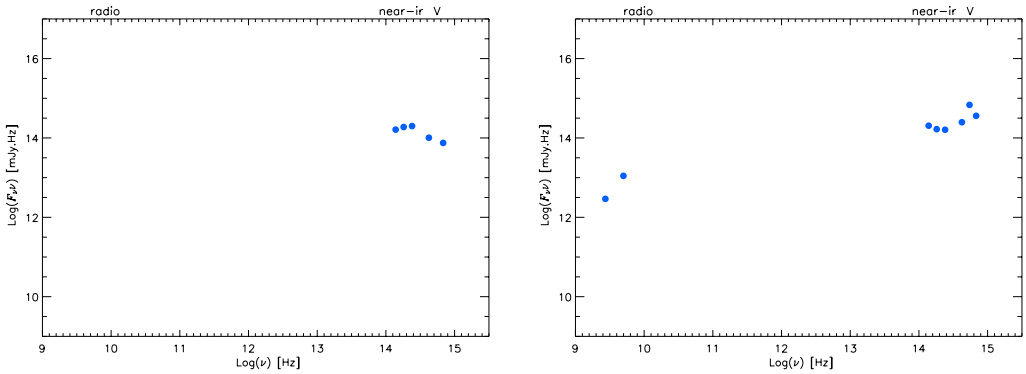

Fig. 26. SED. *Left*: 1129−580 (44a). *Right*: 1144−379 (46a).